Discretization and Algorithms for Strong Coupling in Computational Aeroelasticity[*]

Ralf Massjung
Institut für Geometrie und Praktische Mathematik
RWTH Aachen, Germany
e-mail: massjung@igpm.rwth-aachen.de

January 20, 2003

Contents

1

Abstract

As a model problem of aeroelasticity the panel flutter problem is considered to study the discretization of nonlinear aeroelastic problems and the behaviour of the corresponding algorithmic processes. A discretization that mimics the energy budget of the continuous problem is derived. The set of equations occuring in each time step are implicit in time over fluid and structure and a Newton–Iteration and a Fixed–Point–Iteration are employed as solution methods. Their convergence behaviour is compared. Further, the obtained solutions are compared to the ones found with loose coupling schemes in cases of transonic aeroelasticity, in particular concerning the predicted location of bifurcations.

1 Introduction

The numerical simulation of large scale fluid–structure interaction problems is typically achieved by merging a given fluid code and a given structural code: Due to some coupling strategy, a master program advances the discrete fluid–structure system in time by calling the time stepping modules of fluid and structure and modules that accomplish the data transfer at the interface. The discretization techniques chosen in fluid and structure, the data transfer formulaes and the coupling strategy, define the underlying discrete fluid–structure system and its properties.

Several partitioned procedures, such as the loose coupling [11], the staggered coupling [16], subcycling [18] and predictor corrector strategies [18] have been proposed in the literature. These procedures are known as *partitioned* as they make use of *independent* time integration modules for fluid and structure in order to solve a time dependent aeroelastic problem by appropriately exchanging data between the modules. The only comparison of these partitioned procedures can be found in [8]. In the fluid and in the structural module, several criteria such as conservation properties and order of accuracy are met by diminishing in each time step the residual of appropriately designed sets of discrete equations. But the mentioned coupling strategies barely have the ambitions to do so for the overall aeroelastic scheme. A *conservative load projection* at the fluid–structure interface is discussed in [4] and a *conservative energy transfer* in [9]. In both cases the methods generally only give a conservation property in the data transfer step. But if a fluid module is used that has an at least second order time integrator, as usually is the case, then the conservation in the data transfer step does not automatically imply that the discrete set of equations underlying the numerical scheme possesses a conservation property at the interface. Further, the high time orders present in fluid and structure modules are lost in the proposed schemes. These two unpleasant issues are caused by the coupling schemes employed.

On the other hand, strong coupling schemes are employed in [1] and [17] without attributing interface conservation properties to the proposed schemes.

In contrast to the above approaches, we set up a discrete system for the aeroelastic problem that we prove to mimic the energy conservation property of the continuous problem. Further, all of its discretization steps are of second order in time. The discrete
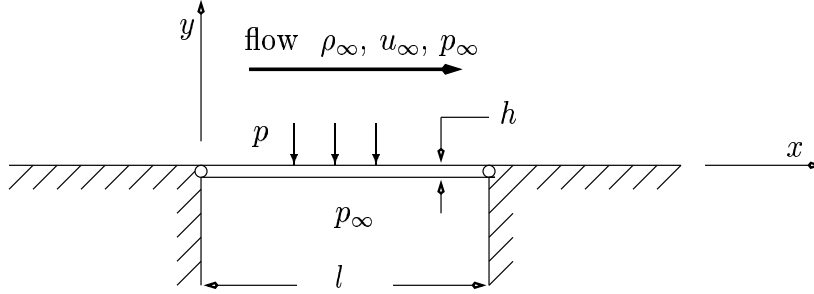
Figure 1: Geometry of the 2D panel–flutter–problem.

equations will be seen to form a set of equations that is implicit in time, coupled over the fluid and structure unknowns. One algorithm employed to drive the equations' residual to zero, is a fixed point iteration which uses several applications of the fluid integrator and the structural integrator within one time step. A second algorithm implemented is a Newton iteration applied to the derived set of fluid structure equations. The experience with algorithms for this nonlinear problem is not yet well developed. Further, a deeper investigation of possible advantages of such a strong coupling methodology over weaker coupling strategies is not yet available. Through numerical experiments we observe that the strong coupling clearly increases the time order in comparison with the loose or staggered coupling.

In section 2, coupling issues will be more thouroughly discussed, using our model problem, the panel flutter problem, as an illustrative example. In section 3 the continuous problem will be formulated. In section 4 the discretization of fluid and structure will be given and the construction of the aeroelastic scheme that satisfies our design criteria will be derived. The solution techniques for the corresponding equations will be discussed in section 5. Finally, in section 6 the proposed schemes and algorithms will be compared in transonic aeroelastic cases, in particular the improvements over the loose coupling when predicting bifurcation points will be shown.

2 Coupling Issues

We wish to make the interrelations of the discretization steps of an aeroelastic problem more precise, taking as a specific example the 2D panel flutter problem with an inviscid flow model. The panel flutter problem consists of a simply supported plate (*panel*) over which a compressible fluid (air) flows. We assume constant behaviour in the direction of the long panel side (spanwise direction), so that a 2D flow passes over a strip of the plate, compare Fig. 1. Let us further specify typical discretization techniques applied in this example: Let the fluid code use cells with piecewise polygonal boundaries, thus a piecewise linear representation of the interface is given for the fluid. In the structure, the typical application of the Finite Element discretization results in a representation of the interface that is a piecewise polynomial of third order. Typically *non-matching* grids appear at the interface, sketched for the present case in Fig. 2. Certain fluid vertices are

3

required to stick to corresponding structural material points at each time level and the remaining fluid grid is deformed accordingly. Let us further assume that the mid-point rule is used in both fluid and structure as a time integrator of second order.

Denote by p_F^n the discrete pressure distribution in the fluid code at time level n, so that $p_F^{n+1/2}$ contributes to advance the fluid from time level n to $n + 1$. Let similarly $p_S^{n+1/2}$ denote the discrete load distribution that enters the structural equations. Let a *projection* of p_F^n onto the structural grid be denoted by $(p_F^n)_S$. Let us further introduce the structural deflection w^n, which defines a fluid grid configuration $\boldsymbol{x}^n$. Let the grid velocities used during the time step from level n to $n + 1$ be denoted by $\dot{\boldsymbol{x}}^{n+1/2}$.

In the popular loose coupling one sets

$$p_S^{n+1/2} \quad := \quad (p_F^n)_S \;, \tag{1}$$

performs a structural time step and determines from the obtained deflection w^{n+1} the grid configuration $\boldsymbol{x}^{n+1}$. Then a fluid time step from t^n to t^{n+1} follows.

Since the mid–point rule was chosen as a time integrator in both fluid and structure, a *conservative load transfer* for the forces in y–direction (n_2 is the normal component in this direction as indicated in Fig. 2 and its value is negative),

$$\int_{\Gamma^{n+1/2}} -p_F^{n+1/2}\, n_2\; ds \quad = \quad \int_0^l p_S^{n+1/2}\; dx \;, \tag{2}$$

is therefore not satisfied for the loose coupling. Further, the time order present in fluid and structural solver is not carried over to the aeroelastic scheme. It is only of first order in time. Here $\Gamma^{n+1/2}$ is the interface belonging to the grid configuration $\boldsymbol{x}^{n+1/2}$ and associated with the time level corresponding to the pressure distribution $p_F^{n+1/2}$. Note that all formulas in this section are on the discrete level and thus in this section the integrals stand for the corresponding quadrature rules employed in the scheme.

In [4] strategies to employ global *load conservation in the projection step* are discussed, i.e. quadrature formulas are required to satisfy

$$\int_{\Gamma^n} -p_F^n\, n_2\; ds \quad = \quad \int_0^l (p_F^n)_S\; dx \;. \tag{3}$$

In [4] numerical experiments were made with a loose coupling, but the time discretizations employed were not discussed. No efforts were made to satisfy a conservative load transfer like (2). Still, drastic improvements over load projections obtained from traditional interpolation methods are found. In the examples of [4], loads with sharp peaks are present, where interpolation violates the conservation properties immensely.

The transfer of geometrical data establishes the *connectivity* of the two media and defines the fluid grid by assigning its boundary position. Further, from the fluid grid positions the fluid grid velocities $\dot{\boldsymbol{x}}^{n+1/2}$ follow.

Together, load and geometry transfer govern the energy exchange of the two media on the discrete level: Global *conservation of the energy*,

$$\int_{\Gamma^{n+1/2}} -p_F^{n+1/2}\, (\dot{\boldsymbol{x}}^{n+1/2})^T \boldsymbol{n}^{n+1/2}\; ds \quad = \quad \int_0^l p_S^{n+1/2}\, \dot{w}^{n+1/2}\; d\xi \tag{4}$$

4

is the most important property to hold on the interface. Here, $\dot{w}^{n+1/2}$ represents the discrete structural velocity that contributes in the energy balance.

Conservation of the energy is also the target of [9]. But in this reference the discussion circumvents the time integrators used in fluid and structure and the resulting demands drawn from (4) upon the coupling schemes. E.g., if methods with at least second oder in time are used, as usually is the case, satisfaction of (4) cannot be achieved with the loose coupling.

Other researchers tackle an improvement of the loose coupling by iteration between fluid and structural solver to achieve converged states of higher order time discretizations at the interface. This is done in [1] and [17] without attributing properties such as (2) or (4) to the proposed schemes. Further, the actual *convergence* in each time step and comparisons with simpler coupling schemes are rarely documented. In [1] an airfoil section with plunge and pitch degree–of–freedom in transonic flow is considered. The iteration method is Jameson's dual time–stepping, where a data–transfer between fluid and structure takes place at each pseudo time step. In [17] a low Mach number flow interacting with an elastically mounted cylinder, where vortex shedding plays an important role, is simulated and considerable improvements over the loose coupling are obtained for large time step sizes. The iteration is a straight forward fixed–point–iteration, alternating several times between fluid and structural solver within one time step, using as data for each medium the most recent obtained in the other medium.

An entirely different approach, that relies on explicit time–integration–schemes, was proposed by Bendiksen [2]. An explicit 5–stage Runge–Kutta–Scheme was applied to the spacially discretized fluid–structure system, exchanging data at each Runge–Kutta stage. It was applied in the transonic regime to the flutter of wing sections and to panel flutter [5], [3]. The main draw back of Bendiksen's method is that it is not applicable when the time step limitations of an explicit scheme are prohibitive, as is often the case, especially in applications involving viscous flow effects.

The design criterion used in the present work is to *mimic the energy conservation properties of the continuous problem on the discrete level*. The continuous model, which in our case does not contain any viscous effects, can be seen to possess the following global energy balance:

$$
\frac{d}{dt}\left(E_F + E_S\right) = \quad \text{power generated at inflow/outflow boundary}
$$
$$
+ \quad \text{power generated by pressure below the panel}
$$

Here E_F, respectively E_S, is the energy contained in the fluid, respectively in the structure. Thus we want to have a discretization that ensures

$$
\frac{E_F^{n+1} + E_S^{n+1} - E_F^n - E_S^n}{\Delta t} = \quad \text{power generated at inflow/outflow boundary}
$$
$$
+ \quad \text{power generated by pressure below the panel.}
$$

This requirement also enforces a conservative energy transfer across the interface as in (4). At the same time we want to have a method where the time order present in fluid
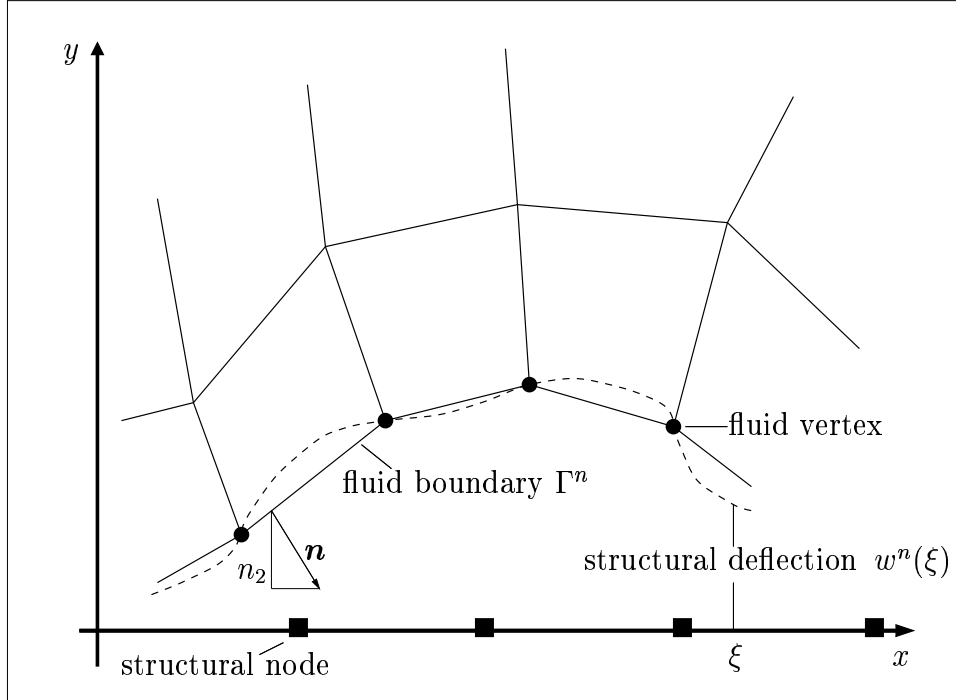
Figure 2: Representation of the interface in fluid and structure

and structural discretization are not reduced in the overall aeroelastic scheme due to "bad" coupling. This is achieved in the sequel by employing a mid–point rule in time over the spacially discretized fluid–structure system and additionally, in order to account for the non–matching grids at the interface, an appropriate quadrature rule is chosen to project the aerodynamic loads onto the panel. Thus, a set of nonlinear equations implicitly coupled over the fluid and structure unknowns results and has to be solved in each time step. This requires appropriate algorithmic tools. The ones employed here are a fixed–point iteration, that successively calls the time integrators of fluid and structure, and a Newton–method that is applied to the nonlinear set of fluid–structure equations.

3   The continuous problem

Our aeroelastic model problem is the panel flutter problem [6]. It is made up of the 2D Euler equations of gas dynamics and a strip of a simply supported von–Karman plate, as described in section 2. It exhibits self–excited oscillations (limit cycle oscillations) caused by the aerodynamic coupling of structural modes. This phenomena is known as *flutter*. Other observed long time behaviours are steady states with either deflected panel (*divergence*) or an undeflected panel (*damped* or *stable* behaviour). Further, the aeroelastic system exhibits a *transonic dip*. This means that the dynamic pressure (kinetic energy of the inflow) needed to obtain unstable behaviour (flutter or divergence) drops

6

considerably to a minimum at an inflow Mach number near unity. Another important feature of panel flutter is that shock movements play a significant role in the unstable mechanisms when the flow is transonic.

The fluid equations are

$$\frac{d}{dt} \int_{\Omega(t)} U \, dx \, dy \; + \; \int_{\partial\Omega(t)} U \, (\boldsymbol{v} - \dot{\boldsymbol{x}})^T \, \boldsymbol{n} \, ds \;\; = \;\; \int_{\partial\Omega(t)} \begin{pmatrix} 0 \\ -p \, n_1 \\ -p \, n_2 \\ -p \, \boldsymbol{v}^T \boldsymbol{n} \end{pmatrix} ds \qquad (5)$$

for arbitraryly moving moving domains $\Omega(t)$. The conservative state vector $U = (\rho, \, \rho \, u, \, \rho \, v,$ $\frac{1}{2} \, \rho \, |\boldsymbol{v}|^2 + \frac{p}{\gamma-1})^T$ is made up of the density ρ, the velocity vector $\boldsymbol{v} = (u, v)^T$ and the pressure p. On a point of the boundary $\partial\Omega(t)$, $\boldsymbol{n} = (n_1, n_2)^T$ is the outward unit normal of $\Omega(t)$ and $\dot{\boldsymbol{x}}$ is the velocity of a boundary point $\boldsymbol{x}(t)$.

For the formulation of the panel equation we introduce the space $V := H^2(0, l) \cap H_0^1(0, l)$. The variational formulation is to find $w(t, x)$ satisfying

$$D \, (w_{xx}, \varphi_{xx}) \; + \; N(w) \cdot (w_x, \varphi_x) \; + \; m \, (\ddot{w}, \varphi) \;\; = \;\; - \, (p_1 - p_2, \varphi) \qquad \forall \, \varphi \in V \, , \qquad (6)$$

where the nonlinear term models a restoring force due to the panel stretching with

$$N(w) \;\; = \;\; \frac{E \, h}{2 \, l} \int_0^l w_x^2 \, dx \, .$$

The constants in the panel equation are the stiffness $D = Eh^3/12(1 - \nu^2)$, the mass per unit area $m = \rho_s h$, the panel thickness h and length l, the density ρ_s, Young's modulus E and the Poisson ratio ν.

Now the aeroelastic problem can be formulated. For convenience, all interface and boundary conditions are given in the strong sense.

- the fluid domain at time t is defined as the space above the deflecting panel and solid wall and is denoted by $\Omega_F(t)$, i.e. for each fluid interface point $\boldsymbol{x}(t)$ associated with a panel point $\xi \in [0, l]$,

$$\boldsymbol{x}(0) \; = \; (\xi, 0)^T, \quad \boldsymbol{x}(t) \; = \; (\xi, w(t, \xi))^T \qquad (7)$$

- for all moving domains $\Omega(t) \subseteq \Omega_F(t)$ (5) holds,

- (6) holds with the r.h.s determined from the fluid pressure on top and p_∞ on the bottom,

$$p_1(t, \xi) \;\; \equiv \;\; p(t, \xi, w(t, \xi)), \qquad \xi \in [0, l] \qquad (8)$$
$$p_2 \;\; \equiv \;\; p_\infty$$

- at infinity we have $\rho = \rho_\infty$, $u = u_\infty$, $v = 0$, $p = p_\infty$,

- on the remaining boundary of $\Omega_F(t)$ the fluid velocity in direction $\boldsymbol{n}$ equals the velocity of the boundary in direction $\boldsymbol{n}$, in particular on the fluid-structure interface,

$$\boldsymbol{v}^T \boldsymbol{n} \;\; = \;\; \dot{\boldsymbol{x}}^T \boldsymbol{n} \;\; = \;\; \dot{w} \, n_2 \qquad (9)$$

Energy equation of the aeroelastic problem

The energy equations for fluid and structure are given by

$$\frac{d}{dt}\, E_F \;\; + \;\; \int_{\partial\Omega_F(t)} \left(\frac{1}{2}\,\rho\,\boldsymbol{v}^2 + \frac{p}{\gamma-1} \right) (\boldsymbol{v} - \dot{\boldsymbol{x}})^T \boldsymbol{n}\; ds \;\;\; = \;\;\; \int_{\partial\Omega_F(t)} -p\,\boldsymbol{v}^T\boldsymbol{n}\; ds\;,$$

$$\frac{d}{dt}\, E_S \;\;\; = \;\;\; \int_0^l (p_2 - p_1)\,\dot{w}\; dx\;,$$

where we have denoted the energy in fluid and structure by

$$E_F(t) \;\;\; \equiv \;\;\; \int_{\Omega_F(t)} \frac{1}{2}\,\rho\,\boldsymbol{v}^2 + \frac{p}{\gamma-1}\;\; d\boldsymbol{x}\;,$$

$$E_S(t) \;\;\; \equiv \;\;\; \int_0^l \frac{m}{2}\,\dot{w}^2 + \frac{D}{2}\,w_{xx}^2\; dx \;\;\; + \;\;\; \frac{E\,h}{2\,l} \left(\frac{1}{2} \int_0^l w_x^2\; dx \right)^2 .$$

The energy equation of the fluid is the fourth component of (5) and the energy equation of the structure is derived by multiplying the strong formulation of (6) by $\dot{w}$ and integrating over the domain.

Summation of the two energy equations yields the energy equation of the aeroelastic system. Here we restrict the fluid solution to a finite domain $\Omega_F(t)$ with non–moving inflow and outflow boundary. Due to the boundary and coupling conditions (7), (8), (9), we end up with

$$\frac{d}{dt}\,(E_F + E_S) \;\;\; = \;\;\; -\int_{\partial\Omega_{F\,in/out}} \left(\frac{1}{2}\,\rho\,\boldsymbol{v}^2 + \frac{p\,\gamma}{\gamma-1} \right) \boldsymbol{v}^T\boldsymbol{n}\; ds \;\; + \;\; \int_0^l p_\infty\,\dot{w}\; dx\;. \quad (10)$$

4 Discretization

4.1 Flow discretization

The flow is discretized in space by the Finite Volume MUSCL scheme on polygonal grids, applying a least–squares linear reconstruction and the Venkatakrishnan limiter on the primitive fluid state vector. As a numerical flux function F we use the van–Leer flux vector splitting for moving edges. Let us write down the discrete flow equations for an inner cell, when employing the mid–point rule in time.

$$|\Omega_i^{n+1}|\,U_i^{n+1} - |\Omega_i^n|\,U_i^n \;\; + \;\; \Delta t \sum_{e_{ij}\subset\partial\Omega_i} |e_{ij}^{n+1/2}|\; F\left(U_{ij}^{n+1/2}, U_{ji}^{n+1/2}, \dot{\boldsymbol{x}}_{ij}^{n+1/2}, \boldsymbol{n}_{ij}^{n+1/2} \right) \;\;\; = \;\;\; 0$$

Here, the fluxes are evaluated at the half time grid position $\boldsymbol{x}^{n+1/2} = (\boldsymbol{x}^{n+1}+\boldsymbol{x}^n)/2$, with the corresponding normal $\boldsymbol{n}_{ij}^{n+1/2}$ and length $|e_{ij}^{n+1/2}|$ of the edge $e_{ij}^{n+1/2}$, which connects the cell Ω_i to its neighbour cell Ω_j. The edge's velocity is given by

$$\dot{\boldsymbol{x}}^{n+1/2} \;\;\; \equiv \;\;\; \frac{1}{2} \left\{ \frac{\boldsymbol{x}_l^{n+1} - \boldsymbol{x}_l^n}{\Delta t} + \frac{\boldsymbol{x}_r^{n+1} - \boldsymbol{x}_r^n}{\Delta t} \right\}$$

and corresponds to the constant velocity by which the edge's mid point can be advanced from its position at time level n to its position at time level $n+1$. Here, $\boldsymbol{x}_l$ and $\boldsymbol{x}_r$ are the two end vertices of an edge. The half time geometry $\boldsymbol{x}^{n+1/2}$ is used to apply reconstruction and limiting on the averaged fluid state $U^{n+1/2} \equiv (U^{n+1} + U^n)/2$ and as a result one obtains the state $U_{ij}^{n+1/2}$ inside the ith cell at the quadrature point of the edge e_{ij}. With this choice the scheme satisfies its discrete geometric conservation law (GCL) [7].

At inflow and outflow boundaries nonreflecting conditions according to [21] are implemented. At impermeable boundaries the flux

$$
|e_{ij}| \cdot F(U_{ij}, \cdot, \dot{\boldsymbol{x}}_{ij}, \boldsymbol{n}_{ij}) \;\; = \;\; |e_{ij}| \, p_{ij} \begin{pmatrix} 0 \\ n_{ij,1} \\ n_{ij,2} \\ \dot{\boldsymbol{x}}_{ij}^T \boldsymbol{n}_{ij} \end{pmatrix} . \tag{11}
$$

is prescribed, which results from the slip-condition $\boldsymbol{v}^T \boldsymbol{n} \;=\; \dot{\boldsymbol{x}}^T \boldsymbol{n}$.

Another time stepping scheme used in the experiments below is the important second order backward differencing scheme. For this scheme the GCL may be satisfied with the choice of edge normals and velocities as given in [14].

4.2   Structural discretization

Conformal elements in one dimension for fourth order operators are constructed from the Hermite shape functions on the unit interval, $\xi \in [0, 1]$,

$$
\begin{aligned}
s_{0,l}(\xi) &= (1 + 2\xi)\,(1 - \xi)^2\,, \\
s_{0,r}(\xi) &= (3 - 2\xi)\,\xi^2\,, \\
s_{1,l}(\xi) &= \xi\,(1 - \xi)^2\,, \\
s_{1,r}(\xi) &= -(1 - \xi)\,\xi^2\,.
\end{aligned}
$$

We have $n-1$ inner nodes, so that $2(n-1)+2$ basis functions $\phi_l(x)$ are constructed from these shape functions when the panel is simply supported. We plug

$$
w(t, x) \;=\; \sum_l \alpha_l(t)\,\phi_l(x)
$$

into (6) and test with the basis functions; further we introduce $\beta_l \equiv \dot{\alpha}_l$ to obtain a first order system of ODEs:

$$
\sum_l D\,\alpha_l\,(\phi_l, \phi_k)_2 \,+\, \alpha_l\,N(w_x)\,(\phi_l, \phi_k)_1 \,+\, m\,\dot{\beta}_l\,(\phi_l, \phi_k)_0 \;=\; -\,(p_1 - p_2, \phi_k)_0 \quad \forall\, k\,,
$$

$$
\dot{\alpha}_k \;=\; \beta_k \qquad \forall\, j\,.
$$

Here, we have used abbreviations for the inner products,

$$
\begin{aligned}
(\phi, \psi)_0 &\equiv (\phi, \psi)\,, \\
(\phi, \psi)_1 &\equiv (\phi_x, \psi_x)\,, \\
(\phi, \psi)_2 &\equiv (\phi_{xx}, \psi_{xx})\,.
\end{aligned}
$$

9

The set of $4(n-1)+4$ ODEs may now be integrated in time with any kind of Runge-Kutta-scheme to approximately solve for discrete values of the coefficients $\alpha_l(t)$, $\beta_l(t)$. The following second order implicit rule will be used below in the construction of an aeroelastic scheme with correct energy transfer:

$$\sum_l D\,\alpha_l^{n+1/2}\,(\phi_l,\phi_k)_2 \;+\; \alpha_l^{n+1/2}\,N^{n+1/2}\,(\phi_l,\phi_k)_1 \;+\; m\,\frac{\beta_l^{n+1}-\beta_l^n}{\Delta t}\,(\phi_l,\phi_k)_0 \;\;=$$

$$= \;\; -\,((p_1-p_2)^{n+1/2},\phi_k)_0 \quad \forall\, j$$

$$\frac{\alpha_k^{n+1}-\alpha_k^n}{\Delta t} \;\;=\;\; \beta_k^{n+1/2} \qquad \forall\, k$$

Here we have set $(...)^{n+1/2} \equiv ((...)^{n+1}+(...)^n)/2$. In particular, the nonlinearity is evaluated with a trapezoidal rule. Defining $w^n(x) \equiv \sum_l \alpha_l^n\,\phi_l(x)$ and introducing the velocity $\dot{w}^n(x) \equiv \sum_l \beta_l^n\,\phi_l(x)$, this system reads

$$\left.\begin{aligned}
N^{n+1/2} &= (N(w^{n+1})+N(w^n))/2 \\
\Delta t\,D\,(w^{n+1/2},\phi_k)_2 \;+\; \Delta t\,N^{n+1/2}\,(w^{n+1/2},\phi_k)_1 \; + & \\
+\; m\,(\dot{w}^{n+1}-\dot{w}^n,\phi_k)_0 &= -\,\Delta t\,((p_1-p_2)^{n+1/2},\phi_k)_0 \\
\alpha_k^{n+1}-\alpha_k^n &= \Delta t\,\beta_k^{n+1/2} \\
&\text{for all } k
\end{aligned}\right\} \quad (12)$$

4.3 Mimicing the energy budget of the continuous problem on the discrete level

By definition of the Finite Volume Method as a conservative scheme, the energy conservation properties are carried over from the continuous to the discrete level in the fluid. In the structure, the choice of the time integrator decides if the energy conservation is reflected correctly in the discrete scheme. Here, after the spacial FEM discretization, the time integration scheme (12) is a scheme with the desired property, as will be seen below. Further, the use of non–matching interface representations has to be taken care of, so that the energy exchange at the interface is conservative. These points will be adressed in the following construction of the aeroelastic scheme. This scheme is constructed such that the energy conservation properties of the continuous problem, compare (10), are mimiced on the discrete level.

Employing the mid-point rule in time, the energy balance for a cell can be written as

$$E_{F,i}^{n+1}-E_{F,i}^n \;\;=\;\; -\Delta t\cdot\sum_{e_{ij}\subset\partial\Omega_i}|e_{ij}^{n+1/2}|\cdot F_4(\mathcal{U}_{ij}^{n+1/2},\mathcal{U}_{ji}^{n+1/2},\dot{\boldsymbol{x}}_{ij}^{n+1/2},\boldsymbol{n}_{ij}^{n+1/2})\;.$$

Here F_4 is the fourth component of the numerical flux F and all its arguments are taken at the edge center. The energy contained in the ith cell at time level n is $E_{F,i}^n = |\Omega_i^n|\cdot$

10

$(\rho_i^n |\boldsymbol{v}_i^n|^2/2 + p_i^n/(\gamma - 1))$. The discrete fluid energy is $E_F^n \equiv \sum_i E_{F,i}^n$. We can divide the energy production into the contribution $\partial E_{FS}^{n+1/2}$ coming from the interface and the contribution $\partial E_F^{n+1/2}$ from the remaining boundary. Thus we have

$$E_F^{n+1} - E_F^n \quad = \quad \partial E_{FS}^{n+1/2} + \partial E_F^{n+1/2} \ .$$

Further the energy flux at impermeable non–moving boundary parts vanishes due to (11). Thus the only contribution remaining in $\partial E_F^{n+1/2}$ comes from inflow and outflow boundaries, so that we can write

$$E_F^{n+1} - E_F^n \quad = \quad \partial E_{FS}^{n+1/2} + \partial E_{in/outflow}^{n+1/2} \ . \tag{13}$$

The energy flux at an interface edge is given by

$$F_4(\mathcal{U}_{ij}^{n+1/2}, \cdot , \dot{\boldsymbol{x}}_{ij}^{n+1/2}, \boldsymbol{n}_{ij}^{n+1/2}) \quad \equiv \quad p_{ij}^{n+1/2} \, (\dot{\boldsymbol{x}}_{ij}^{n+1/2})^T \boldsymbol{n}_{ij}^{n+1/2} \ ,$$

and summing over all edges on the interface, we obtain

$$\partial E_{FS}^{n+1/2} \quad \equiv \quad -\Delta t \sum_{e_{ij} \subset \Gamma_{FS}} |e_{ij}^{n+1/2}| \cdot p_{ij}^{n+1/2} \, (\dot{\boldsymbol{x}}_{ij}^{n+1/2})^T \boldsymbol{n}_{ij}^{n+1/2} \ .$$

Let us look at a single edge $e \equiv \overline{\boldsymbol{x}_l \, \boldsymbol{x}_r} \subset \Gamma_{FS}$ with end vertices $\boldsymbol{x}_l, \boldsymbol{x}_r$, omitting the ij-indices for the moment, compare Fig. 3. Then $\dot{\boldsymbol{x}}^{n+1/2}$ is given by

$$\dot{\boldsymbol{x}}^{n+1/2} \quad \equiv \quad \frac{1}{2} \left\{ \frac{\boldsymbol{x}_l^{n+1} - \boldsymbol{x}_l^n}{\Delta t} + \frac{\boldsymbol{x}_r^{n+1} - \boldsymbol{x}_r^n}{\Delta t} \right\} \ .$$

Further from $\boldsymbol{x}_l^n = (\xi_l, w_l^n)^T$, $w_l^n \equiv w^n(\xi_l)$ for some $\xi_l \in [0, l]$, and correspondingly for the right point $\boldsymbol{x}_r^n$, we get

$$(\dot{\boldsymbol{x}}^{n+1/2})^T \boldsymbol{n}^{n+1/2} \quad = \quad \frac{1}{2} \left\{ \frac{w_l^{n+1} - w_l^n}{\Delta t} + \frac{w_r^{n+1} - w_r^n}{\Delta t} \right\} n_2^{n+1/2} \ .$$

Looking again at specific edges, adding the indices ij, using $|e_{ij}^{n+1/2}| = -(\xi_{r,ij} - \xi_{l,ij})/n_{2,ij}^{n+1/2}$ and denoting $\Delta \xi_{ij} \equiv \xi_{r,ij} - \xi_{l,ij}$, we obtain

$$\partial E_{FS}^{n+1/2} \quad = $$
$$= \quad \Delta t \sum_{e_{ij} \subset \Gamma_{FS}} \Delta \xi_{ij} \, p_{ij}^{n+1/2} \frac{1}{2} \left\{ \frac{w^{n+1}(\xi_{l,ij}) - w^n(\xi_{l,ij})}{\Delta t} + \frac{w^{n+1}(\xi_{r,ij}) - w^n(\xi_{r,ij})}{\Delta t} \right\} \ . \tag{14}$$

We turn to the discrete panel equations (12) and have to specify the load term due to the coupling conditions and its evaluation through a quadrature rule, which we choose as

$$-\Delta t \left((p_1 - p_2)^{n+1/2}, \phi_k \right)_0 \quad = \quad -\Delta t \left(p(\xi, w^{n+1/2}(\xi)) - p_\infty, \phi_k(\xi) \right)_0 \quad \approx$$
$$\approx \quad -\Delta t \sum_{e_{ij} \subset \Gamma_{FS}} \Delta \xi_{ij} \, (p_{ij}^{n+1/2} - p_\infty) \left\{ \phi_k(\xi_{l,ij}) + \phi_k(\xi_{r,ij}) \right\} /2 \ . \tag{15}$$

Note that most summands do not contribute anything since $\xi_{l,ij}, \xi_{r,ij} \notin \text{supp}(\phi_k)$ in most cases. For the inner products on the l.h.s. of (12) we may use a different quadrature rule, let us assume that this rule is exact. Plugging the quadrature formula (15) into (12), multiplying the resulting equation with $\beta_k^{n+1/2} = (\alpha_k^{n+1} - \alpha_k^n)/\Delta t$ and summing over all k we obtain

$$\Delta t\, D\,(w^{n+1/2}, \dot{w}^{n+1/2})_2 + \Delta t\, N^{n+1/2}\,(w^{n+1/2}, \dot{w}^{n+1/2})_1 + m\,(\dot{w}^{n+1} - \dot{w}^n, \dot{w}^{n+1/2})_0 \quad =$$

$$= \quad -\Delta t \sum_{e_{ij} \subset \Gamma_{FS}} \Delta\xi_{ij}\,(p_{ij}^{n+1/2} - p_\infty) \frac{1}{2} \left\{ \frac{w^{n+1}(\xi_{l,ij}) - w^n(\xi_{l,ij})}{\Delta t} \quad + \right.$$

$$\left. + \quad \frac{w^{n+1}(\xi_{r,ij}) - w^n(\xi_{r,ij})}{\Delta t} \right\} .$$

From the third equation of (12) we have

$$w^{n+1} - w^n \quad = \quad \Delta t\, \dot{w}^{n+1/2} .$$

Differentiating s times with respect to x, multiplying by $\alpha_k^{n+1/2} \phi_k$, respectively its derivatives, summing over all k and integrating, gives

$$\frac{1}{2}\,(w^{n+1} - w^n, w^{n+1} + w^n)_s \quad = \quad \Delta t\,(\ddot{w}^{n+1/2}, w^{n+1/2})_s \qquad \text{for} \quad s = 0, 1, 2\,,$$

or

$$\frac{1}{2}\,\left\{(w^{n+1}, w^{n+1})_s - (w^n, w^n)_s\right\} \quad = \quad \Delta t\,(\dot{w}^{n+1/2}, w^{n+1/2})_s \qquad \text{for} \quad s = 0, 1, 2\,.$$

Note that $N^{n+1/2} = \frac{E\,h}{2\,l}\,\left\{(w^{n+1}, w^{n+1})_1 + (w^n, w^n)_1\right\}/2$ and thus

$$\Delta t\, N^{n+1/2}\,(w^{n+1/2}, \dot{w}^{n+1/2})_1 \quad = \quad \frac{E\,h}{2\,l}\,\frac{(w^{n+1}, w^{n+1})_1 + (w^n, w^n)_1}{2}\,\frac{(w^{n+1}, w^{n+1})_1 - (w^n, w^n)_1}{2}$$

$$= \quad \frac{E\,h}{2\,l}\,\frac{(w^{n+1}, w^{n+1})_1^2 - (w^n, w^n)_1^2}{4} \quad .$$

With the discrete panel energy

$$E_S^n \quad \equiv \quad \frac{m}{2}\,(\dot{w}^n, \dot{w}^n)_0 + \frac{E\,h}{2\,l}\,\left(\frac{(w^n, w^n)_1}{2}\right)^2 + \frac{D}{2}\,(w^n, w^n)_2\,,$$

the energy change on the discrete level is

$$E_S^{n+1} - E_S^n \quad =$$

$$= \quad \sum_{e_{ij} \subset \Gamma_{FS}} \frac{\Delta\xi_{ij}\,(p_\infty - p_{ij}^{n+1/2})}{2}\,\left\{w^{n+1}(\xi_{l,ij}) - w^n(\xi_{l,ij}) + w^{n+1}(\xi_{r,ij}) - w^n(\xi_{r,ij})\right\} . \tag{16}$$

Now, from (13), (14), and (16) we see that in the energy change of the discrete fluid-structure-system, $E_F^{n+1} + E_S^{n+1} - (E_F^n + E_S^n)$, the contributions from the interface cancel, so that the following theorem holds:
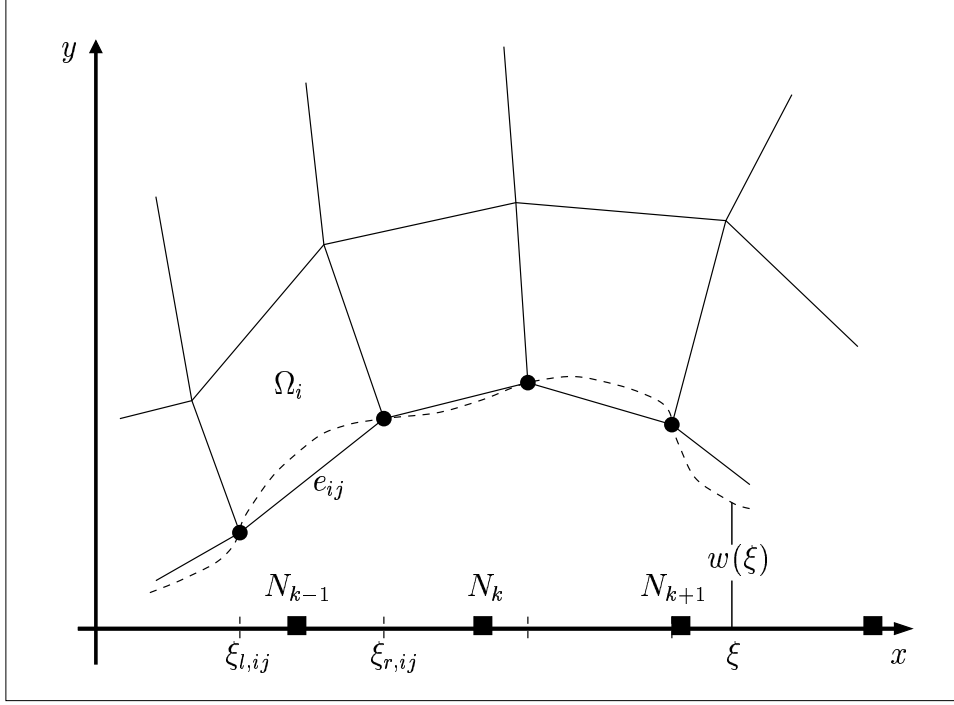
12

Figure 3: Representation of the interface in fluid and structure, the N_j are panel nodes.

Theorem: The numerical scheme

$$
\left.
\begin{aligned}
&|\Omega_i^{n+1}|\, U_i^{n+1} \;-\; |\Omega_i^n|\, U_i^n \;+\; \\
&\qquad +\;\; \Delta t \sum_{e_{ij} \subset \partial \Omega_i} |e_{ij}^{n+1/2}|\, F(U_{ij}^{n+1/2}, U_{ji}^{n+1/2}, \dot{\boldsymbol{x}}_{ij}^{n+1/2}, \boldsymbol{n}_{ij}^{n+1/2}) \;\;=\;\; 0\,, \\
&\qquad \text{with the boundary treatment (11)}, \\
&\boldsymbol{x}_{l,ij}^n \;=\; (\xi_{l,ij}, w^n(\xi_{l,ij}))^T\,, \quad \boldsymbol{x}_{r,ij}^n \;=\; (\xi_{r,ij}, w^n(\xi_{r,ij}))^T \\
&\qquad \text{for all flow edges } e_{ij} \text{ on the panel},
\end{aligned}
\right\}
\tag{17}
$$

$$
\left.
\begin{aligned}
&\Delta t\, D\left(w^{n+1/2}, \phi_k\right)_2 \;+\; \Delta t\, N^{n+1/2}\left(w^{n+1/2}, \phi_k\right)_1 \;+\; m\left(\dot{w}^{n+1} - \dot{w}^n, \phi_k\right)_0 \;\;=\; \\
&\qquad =\;\; -\,\Delta t \sum_{e_{ij} \subset \Gamma_{FS}} \Delta \xi_{ij}\, p_{ij}^{n+1/2}\, \{\phi_k(\xi_{l,ij}) + \phi_k(\xi_{r,ij})\}\, /2 \qquad \forall\, k\,, \\
&\alpha_k^{n+1} - \alpha_k^n \;\;=\;\; \Delta t\, \beta_k^{n+1/2} \qquad \forall\, k\,,
\end{aligned}
\right\}
\tag{18}
$$

approximating the aeroelastic initial-boundary-value-problem of section 3, satisfies the GCL in the fluid and carries over the energy balance from the continuous level (10) to the discrete level. All its time discretization steps are of second order.

5   Algorithms

An algorithm that solves the discrete flow equations (17) with a prescribed boundary movement, may serve as a fluid time integrator. Similarly, a structural time integrator
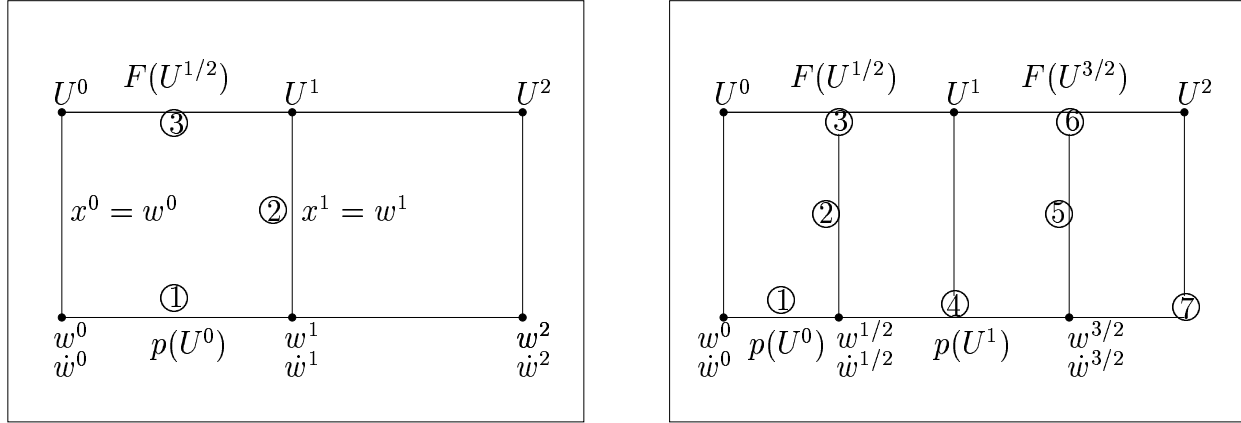
Figure 4: Loose Coupling (left) and Staggered Coupling (right). In the Staggered Coupling, in step 2, the grid position of time level 1 is determined by $x^1 = x^0 + \Delta t\, \dot{w}^{1/2}$ and accordingly, in step 5, the grid position of time level 2 is determined by $x^2 = x^1 + \Delta t\, \dot{w}^{3/2}$.

is given if the equations (18) can be solved when a load is prescribed. In both cases our solution strategy is a matrix–free Newton–GMRes method. With the resulting fluid time integrator and structural time integrator, the aeroelastic problem can be tackled with all partitioned schemes. Amongst the partitioned schemes we have implemented, are the loose coupling, the staggered coupling and a strong coupling scheme that solves the coupled set (17) & (18) via a fixed point iteration. The latter method applies the fluid integrator and the structural integrator several times within one time step. They are successively applied in the sequence given by the loose coupling with the purpose of diminishing the residual of the coupled system (17) & (18). The loose coupling and the staggered coupling are schematically depicted in Fig. 4. In the figure the time axis goes from left to right and the first three time levels are shown. The encircled numbers give the order in which structural time integration (bottom line), fluid grid movement (vertical lines) and fluid time integration (top line) are performed. Further, we have indicated from which time level the fluid pressure is taken as the load to perform a structural time integration. Further, we have indicated how the grid position is transferred at the interface from structure (w) to fluid (x) in order to move the grid. As an example for a higher order time integrator in the fluid we have chosen the mid–point rule and indicated from which time level the fluid flux is taken.

The matrix–free Newton–GMRes solves a nonlinear system $G(x) = 0$ by applying a Newton iteration and employing GMRes [20] as a linear solver. Since the GMRes iteration only needs to know the evaluation of matrix vector products $G'(x^*)x$, with the Jacobian G', the determination and storage of G' may be avoided by approximating

$$G'(x^*)\,x \quad \approx \quad \frac{G(x^* + \epsilon\, x) - G(x^*)}{\epsilon} \; .$$

Here ϵ should be chosen big enough to avoid cancellation and small enough to keep the

14

approximation accurate. In all matrix–free Newton–GMRes iterations we have used

$$\epsilon \quad = \quad \frac{\mathrm{eps}^{1/2}}{||x||_2} \qquad \text{where eps is the machine-accuracy,}$$

which was also recommended in [19]. To accelerate convergence in the linear solvers, a block symmetric Gauss–Seidel preconditioner based on a first order spacial discretization is used in the fluid, whereas a block symmetric Jacobi preconditioner is used in the structure.

Further, we propose to achieve a strong coupling by applying the matrix–free Newton–GMRes method to the discrete fluid–structure system (17) & (18). The discrete fluid–structure system may be written in compact form as

$$\mathcal{H}(\mathcal{U}^{n+1}, \mathcal{W}^{n+1}; \mathcal{U}^n, \mathcal{W}^n) \quad \equiv \quad \left(\begin{array}{c} \mathcal{H}_F(\mathcal{U}^{n+1}, \mathcal{W}^{n+1}; \mathcal{U}^n, \mathcal{W}^n) \\ \mathcal{H}_S(\mathcal{U}^{n+1}, \mathcal{W}^{n+1}; \mathcal{U}^n, \mathcal{W}^n) \end{array} \right) \quad = \quad 0 \, .$$

Here the states of fluid $\mathcal{U}^n$ and structure $\mathcal{W}^n$ at the beginning of the time step are given. We have to solve for $\mathcal{U}^{n+1}$ and $\mathcal{W}^{n+1}$. In the evaluation of the structural equations $\mathcal{H}_S$ only the pressures from the fluid states $\mathcal{U}^{n+1}$, $\mathcal{U}^n$ are needed to determine the loads, whereas in $\mathcal{H}_F$ only the deflections from $\mathcal{W}^{n+1}$, $\mathcal{W}^n$ are needed to determine the fluid grid positions at the new and old time level. An evaluation of $\mathcal{H}$ proceeds as follows – the fluid grid movement is shortly discussed at the end of this section:

- determine the new grid from $\mathcal{W}^{n+1}$
- determine the grid velocities
- reconstruction and limitation of the fluid state $\mathcal{U}^{n+1/2}$
- determine the fluxes
- $\mathcal{H}_\mathcal{F}$ is given according to (17)
- from the reconstructed pressure determine the structural load
- $\mathcal{H}_S$ is given according to (18)

In principle, this evaluation of the nonlinearity is all we need to apply the matrix–free Newton GMRes iteration. The issue of preconditioning is adressed in a decoupled fashion. This means that a preconditioning step to approximately solve $\mathcal{H}' \cdot (\mathcal{V}_F, \mathcal{V}_S)^T = (b_F, b_S)^T$ consists of applying the fluid preconditioner to the r.h.s. b_F to obtain $\mathcal{V}_F$ and the structural preconditioner to the r.h.s. b_S to obtain $\mathcal{V}_S$.

Convergence criterion for strong coupling

As an initial guess for the strong coupling, the result of a loose coupling step is used. The loose coupling first solves the structural equations with the *wrong* fluid load and then solves the fluid equations due to the obtained structural deflections. Thus the structural equations of the loose coupling and of (18) do not coincide, whereas the fluid equations of the loose coupling and of (17) do coincide. This means that, when plugging the initial

guess into the system (17) and (18), the error is only visible in the residual of the structural equations. Thus, the convergence criterion is to reduce the structural residual below a given threshold. If the residual threshold in the fluid equation is already small enough in the initial guess, then a stagnation of the fluid residual in the strong coupling iteration can be accepted. These considerations hold for the strong coupling via fixed point iteration as–well as via the Newton–iteration.

Unfortunately, sometimes a considerable increase in the fluid residual can be observed. A device we propose to enforce the reduction of both residuals in the Newton iteration, is to weight the residuals of fluid and structure within the iteration process, such that they are of equal size in the initial guess. We call this version of the Newton iteration to achieve a strong coupling the *Weighted Newton method*.

Grid movement

In general applications, the grid movement algorithm, which assigns the vertex positions according to the given boundary movement, may require the solution of a system of equations as–well. In our case, the computational domain has a simple geometry, also when it deforms in the aeroelastic simulation. A simple algebraic rule to stretch the grid suffices and is implemented here.

6   Numerical experiments

Our main interest is the behaviour of different coupling schemes with respect to Δt. Therefore a sufficiently accurate spacial resolution of 80 fluid cells on the panel and 26 panel nodes was chosen for all computations presented, compare [5], [10], [12]. In total the fluid grid consists of 8998 quadrilateral cells, reaching the in– and outflow boundaries at 6 panel lengths away from the panel. Away from the panel, the cells are stretched towards the in– and outflow boundaries.

Throughout we use aluminium as panel material, thus fixing the panel parameters $\rho_s = 2700 \ kg/m^3$, $E = 7.1 \cdot 10^{10} \ Pa$ and $\nu = 0.34$. In the dimensionless form all coefficients of the panel equation are determined, when the ratio h/l is specified, which will be done in each of the following cases. The fluid parameters may be defined in two ways: Either we assign the inflow Mach number M_∞, the fluid structure mass ratio $\mu \equiv \rho_\infty l/(\rho_s h)$ and the dimensionless dynamic inflow pressure $\lambda \equiv \rho_\infty u_\infty^2 l^3/D$ or we assign M_∞ and all remaining flow conditions as those found in the atmosphere at a certain altitude.

6.1   Transonic and supersonic panel flutter

Let us first envision some qualitative properties of the flutter solutions. We look at a transonic flutter case with $M_\infty = 1$, $h/l = 0.004537$, $\mu = 0.1$, $\lambda = 260$ and a supersonic flutter case defined through $h/l = 0.004$ and an inflow of $M_\infty = 1.2$ at 20000 feet altitude.
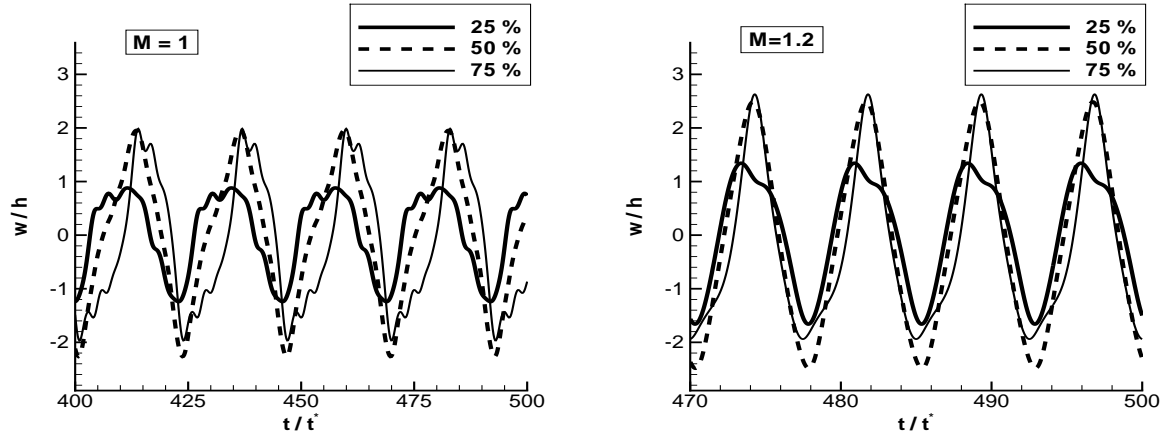
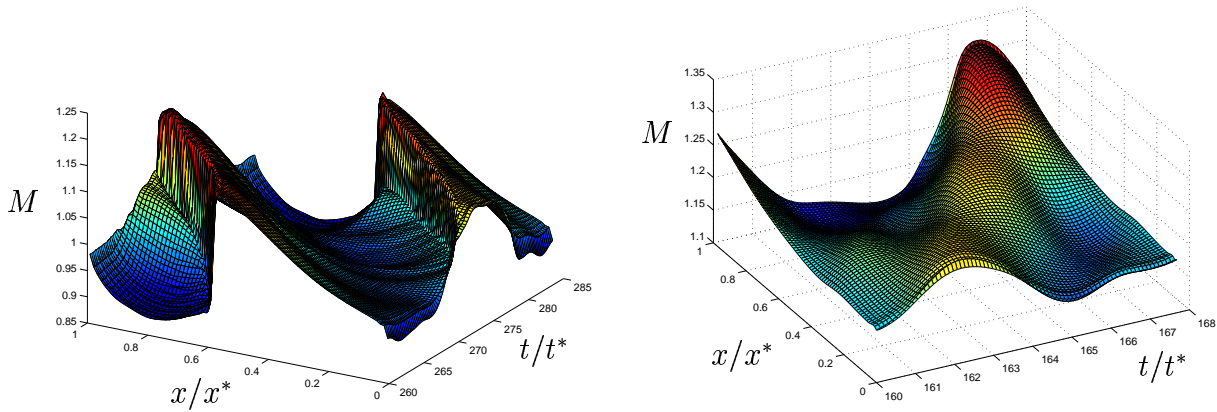Figure 5: The panel deflections at various points on the panel.

Figure 6: Mach numbers along the panel during one period of the limit cycle

These cases were also considered in [5]. The periodic panel deflections resulting in these cases are visualized in Fig. 5 by the deflection at 25%, 50% and 75% chord of the panel.

In Fig. 6 the development of the Mach number distribution on the panel over a flutter cycle is shown. We can observe that the Mach number on the panel has a moving shock in the limit cycle in the transonic case, whereas in the supersonic case the fluid quantities are smooth along the panel. In the supersonic case shocks periodically build up and disappear at the trailing and the leading edge. Higher harmonics in the panel deflection are more pronounced in the transonic case in contrast to the supersonic case. In the transonic case we can relate the shock speed to the CFL number in the fluid, and for the given grid, at a CFL number of 35, the shock moves about one cell during a time step. Further, this CFL number corresponds to 112 time steps per flutter period.
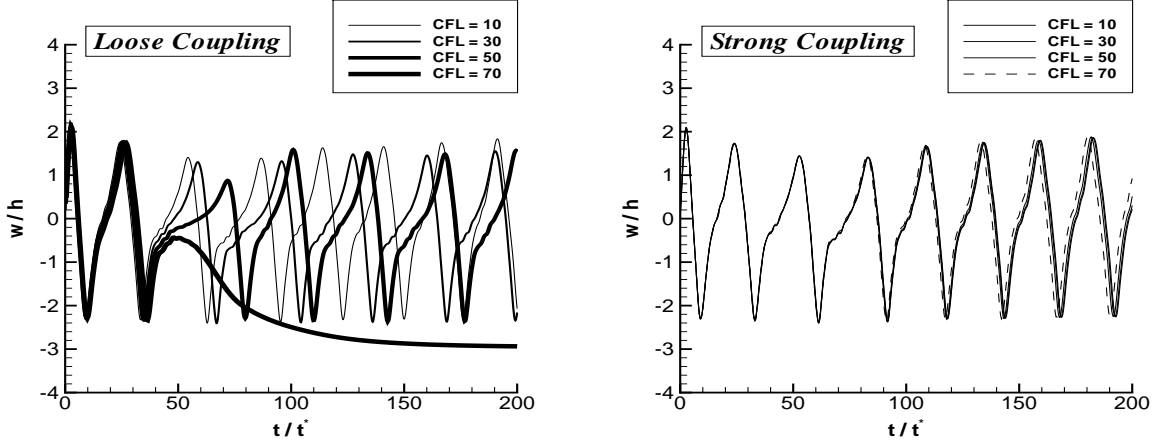
Figure 7: Panel mid point deflection for loose and strong coupling at different Δt.

6.2 Flutter at $M_\infty = 1$

The transonic flutter case described in the above section is considered. Here we compare the behaviour of the solutions obtained with the loose and the strong coupling as $\Delta t \to 0$. As the strong coupling algorithm we use the FPI with a loose coupling step as initial guess and require the structural residual to drop by one order of magnitude. Increasing the fluid CFL number from 10, 30, 50 to 70, we can observe in Fig. 7 how time accuracy is lost in the loose coupling. We even obtain a bifurcation from flutter to divergence, when changing from CFL = 50 to CFL = 70. In contrast, the results obtained with strong coupling remain very good in accuracy even at a CFL number of 70. A direct comparison in Fig. 8 further shows the continuing improvement of the loose coupling in accuracy when decreasing the CFL number to 0.7, whereas the strong coupling's solution at CFL = 50 has *the* same accuracy. The staggered scheme delivers plots that look very similar to the one given for the loose coupling.

Let us further note, that the bifurcation observed in the loose coupling when changing from CFL = 50 to CFL = 70 at $\lambda = 260$ considerably overestimates the bifurcation point. Using the strong coupling, a bifurcation from divergence to flutter can be observed at $M_\infty = 1$ when we increase the nondimensional dynamic pressure from $\lambda = 160$ to $\lambda = 170$.

One may also ignore the time accuracy of the solutions and shift the interest to the obtained periodic behaviour. Some quantities characterizing the flutter cycle are the flutter period and the amplitudes. In Fig. 9 we compare the periods and negative amplitudes of the flutter cycles resulting from the loose and strong coupling when decreasing the CFL number. We observe very fast convergence in the flutter period with the strong coupling in contrast to the loose coupling. The strong coupling's superiority is less pronounced when considering the negative amplitude. As the loose coupling exhibits the bifurcation above CFL = 50, as indicated in the picture, a quantitative comparison does not make sense.
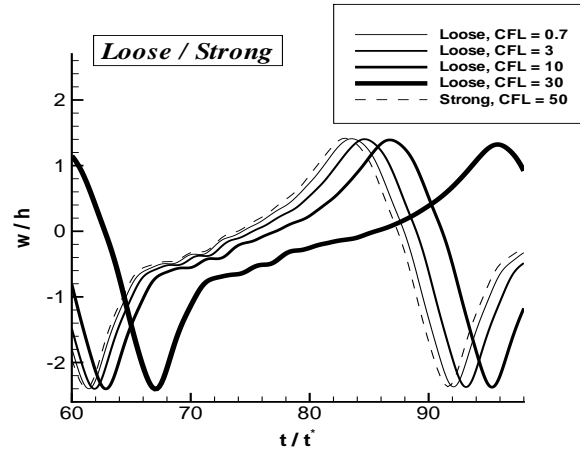
18

Figure 8: Panel mid point deflection of strong coupling at CFL = 50 compared with result of loose coupling at various CFL numbers.
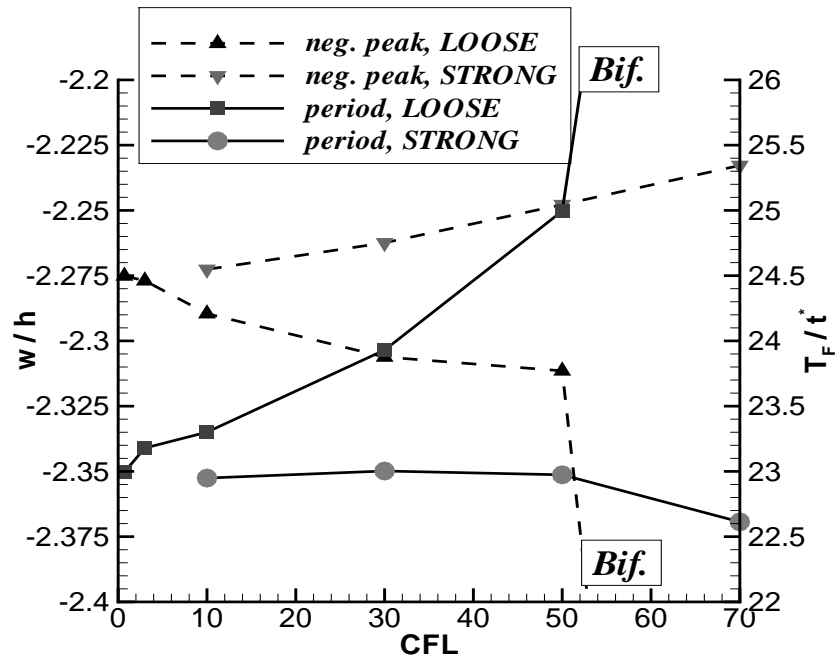

Figure 9: Transonic flutter, convergence in amplituide and period with respect to Δt.

19

6.3 Flutter at $M_\infty = 1.2$

A separation of the solutions, as observed in the transonic case for the loose coupling (Fig. 7), does not occur in this supersonic flutter case. As seen before, here the fluid data remains smooth along the panel. A calculation with CFL = 55, which corresponds to

λ\CFL	L 0.7	L 7	L 20	L 50	ST 0.7	ST 7	ST 20	ST 50	FPI 7	FPI 20	FPI 50	N/W 7	N/W 20	N/W 50	N 7	N 20	N 50
3600				F				F									
3500				F				D									
3400				D				D									
3300				D													
3200			F				F										
3100			F				F										
3000		F	D			F	D										
2900	F	F	D		F	F	D										
2800	F	D			F	D			F	F	F	F		F	F		
2700	D	D			D	D			F	F	F	F	F	F	F		F
2600	D				D				D	D	D	D	F	D	D	F	F
2500									D	D	D	D	D	D	D	F	D
2400													D			D	D

Figure 10: Increasing λ at fixed $M_\infty = 0.95$ we have a bifurcation from divergence (D) to flutter (F). The bifurcation point is determined with the loose coupling (L), the staggered coupling (ST), and the strong coupling via fixed point iteration (FPI), weighted Newton iteration (N/W) and (unweighted) Newton iteration (N) at various CFL numbers.

only 20 time steps per flutter period, determines the amplitudes and flutter periods with a relative error of less than 5% for all coupling schemes. Improvements due to strong coupling can hardly be noticed in this case.

6.4 A bifurcation at $M_\infty = 0.95$

Another numerical experiment in the transonic regime addresses the determination of a bifurcation point with different coupling schemes, algorithms and time step sizes. Increasing the dynamic pressure at fixed Mach number a bifurcation from divergence to flutter occurs, where strong shocks move along the panel in the flutter solution. An aluminium panel with $h/l = 0.002$ is considered and we fix $M_\infty = 0.95$ and $\mu = 0.1$. The nondimensional dynamic pressure is varied in the range $2400 \leq \lambda \leq 3600$. The qualitative results obtained are shown in the table of Fig. 10 and reveal a strong variation of the bifurcation point depending on the coupling scheme, when using moderate CFL numbers. Here, a CFL number of 50 corresponds to 115 time steps per flutter period. Clearly, the loose coupling overestimates the dynamic pressure at the bifurcation point immensely at CFL = 50 and does not seem to be converged yet at CFL = 10. At CFL = 50, the strong coupling via fixed point iteration (FPI) has already converged in the quantity of interest. The strong coupling via Newton–iteration shows slight variations as CFL is reduced from 50 to 10.

Note also, that using a strong coupling scheme, the change to flutter is detected at $\lambda = 2500$ in [10].

Convergence histories

We have picked the case with $\lambda = 2700$ at CFL = 20 to compare the different strong coupling algorithms. In Fig. 12 the behaviour of the structural residual over a range of 1500 time steps can be seen. After each fluid–structure loop the residual is plotted in the diagram. At each time step we have at least two entries, the one from the initial guess and the one from the following iteration loop. For example, in case of the FPI the initial guess, stemming from a loose coupling step, lies around $10^{-1.5}$. This can be red off from the accumulation of dots producing a wavy shape on top of the diagram, whereas after a single FPI iteration the residual is around $10^{-3.5}$, as red off from the wavy shape on the bottom. A similar behaviour can be found for the Newton iteration and the weighted Newton iteration, indicating less regular behaviour and some trouble between time steps 400 and 500. A close–up look, Fig. 11, reveals what actually happens: Throughout, the FPI reduces the structural residual below 10^{-3}, whereas the Newton iterations are less reliable. In order to see this the residuals are connected in order of appearance in the calculation, e.g. the first residual in time step 447, the one from the inital guess, is the one that is connected to the last residual of time step 446 and lies around $10^{-1.5}$ for the weighted Newton method. The iteration does not converge in time step 447, as the last residual is around 1. From the symbol marking this residual a connection is drawn to the residual in the initial guess of time step 448, and so on. Similar convergence problems
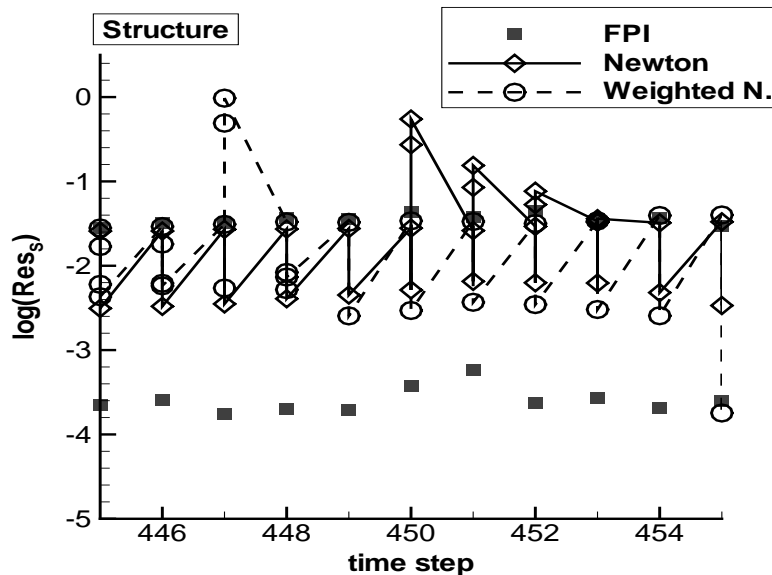
Figure 11: Close–up of structural residual

can be found in time steps 450 to 454 for the (unweighted) Newton method.

Analogous plots for the fluid residuals can be found in Fig. 13 and Fig. 14. As mentioned before, a stagnation in the fluid residual may be accepted. We can observe in Fig. 13 that the FPI keeps the fluid residual below 10^{-7}, the assigned threshold in the fluid solver. The Newton method frequently pushes the fluid residual towards 10^{-6}; the residual of its initial guess is always below 10^{-7}. Finally, we observe that the weighting in the Newton method works well, keeping the residual below 10^{-7} except for two outliers. In Fig. 14 we clearly see that in the (unweighted) Newton iteration, the fluid residual grows, whereas in the weighted Newton iteration the fluid residual drops (except for two outliers in the observed 1500 time steps).

As a conclusion, the FPI seems to offer the best compromise. It is robust, reducing the significant residual, namely the structural residual, fastest, keeping the fluid residual sufficiently low. In contrast, the (unweighted) Newton shows convergence problems in a few time steps, with considerable increases in fluid residual. The latter may be avoided by weighting the Newton iteration. But let us note that the weighted Newton iteration needs about three times as much GMRes iterations than the (unweighted) Newton method.

Going back to the table (Fig. 10) discussed above, these observations for the convergence histories seem to have a noticeable effect on the obtained solutions. The FPI seems to predict the bifurcation correctly at the largest time step size.
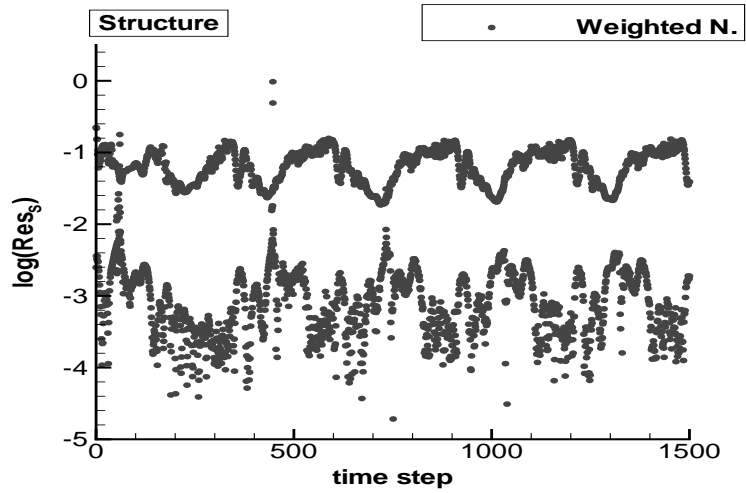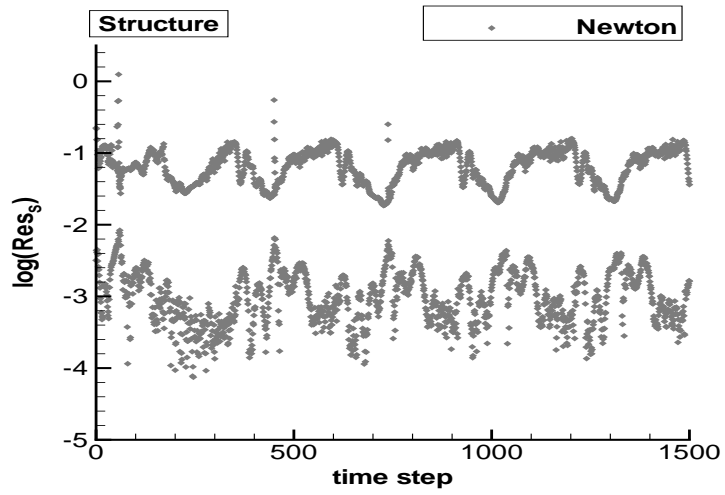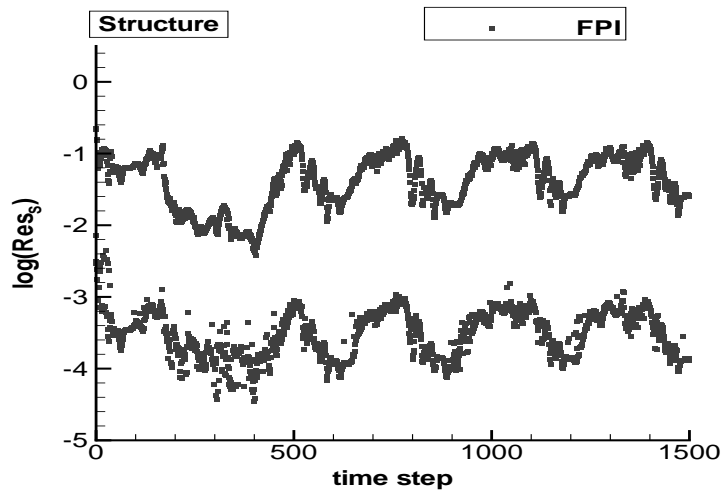
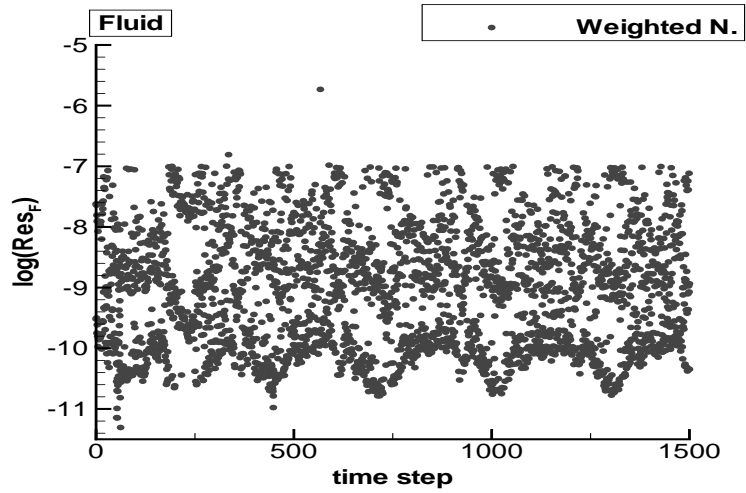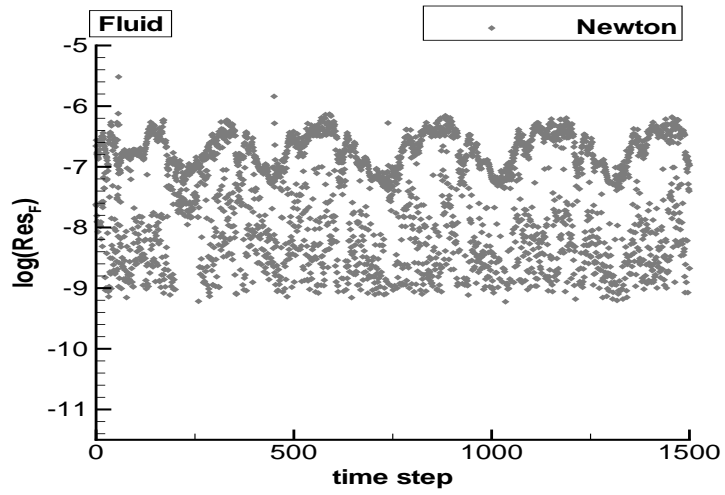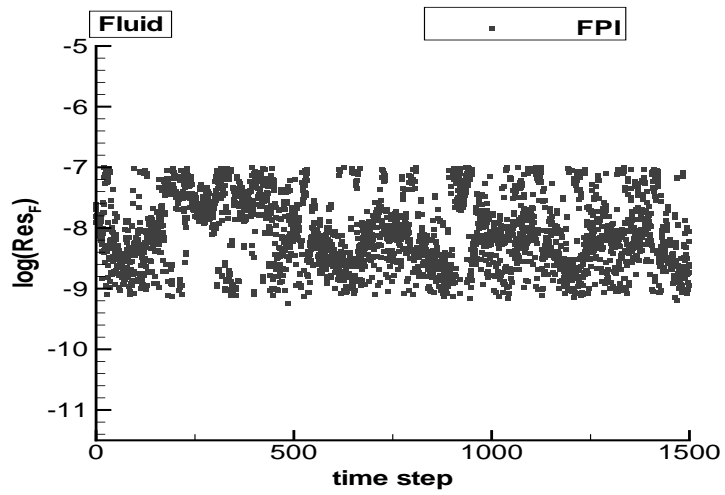Figure 12: Behaviour of structural residual over 1500 time steps.

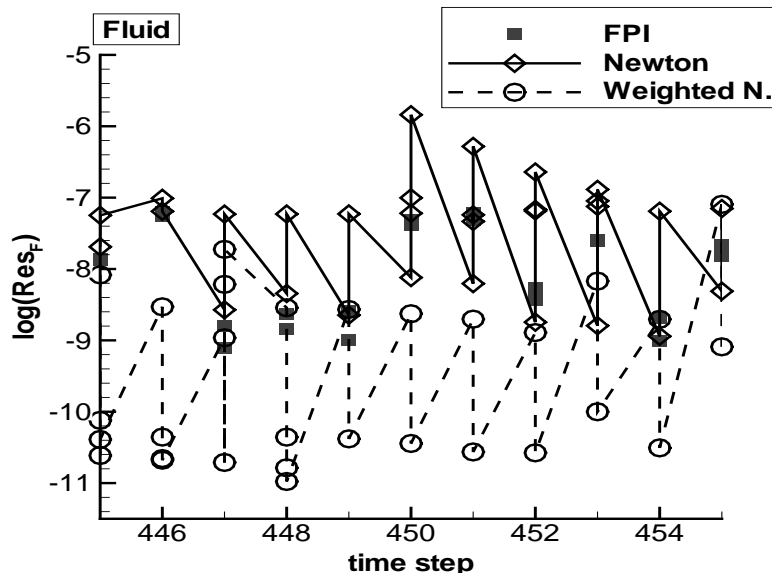Figure 13: Behaviour of fluid residual over 1500 time steps.

Figure 14: Close–up of fluid residual

6.5 Stability chart

We consider the case of a simply supported aluminium panel of thickness $h/l = 0.004537$ in a flow of air with fluid–structure mass ratio of $\mu = 0.1$. The corresponding stability boundary was determined numerically in [5] and reconfirmed in [12].

In Fig. 15, we see that we have agreement with the result of [5] in the subsonic range, but a clear deviation for Mach numbers above 1. The result was obtained with the strong coupling and CFL = 50. At CFL = 10 the same stability boundary results. With the loose coupling, all computations performed to produce the stability boundary seemed to predict the same long time behaviour as the strong coupling. But in all computations, after the long time behaviour seemed to be reached, a numerical instability was triggered in the loose coupling. These instabilities will be shown in the following section.

Still it is not clear what to attribute to the deviations from the results of [5]. The different amount of numerical diffusion used in the fluid solver may be a reason.

6.6 Numerical instabilities with loose coupling

Trying to determine the stability boundary of the previous section with the loose coupling, we have encountered numerical long time instabilities. Such instabilities are also observed in [10]. When the solution seems to have reached its long time behaviour, a numerical instability is triggered. The instability seems to occur the sooner the larger the time lag is between the pressures acting on fluid and panel. Namely, using the second order BDF in the fluid and the trapezoidal rule in the panel, we have a time lag of Δt and the instability typically occurrs around a dimensionless time $t/t^* = 1000$. The instability causes the panel to oscillate with growing amplitudes. Around $t/t^* = 3000$ the algorithm
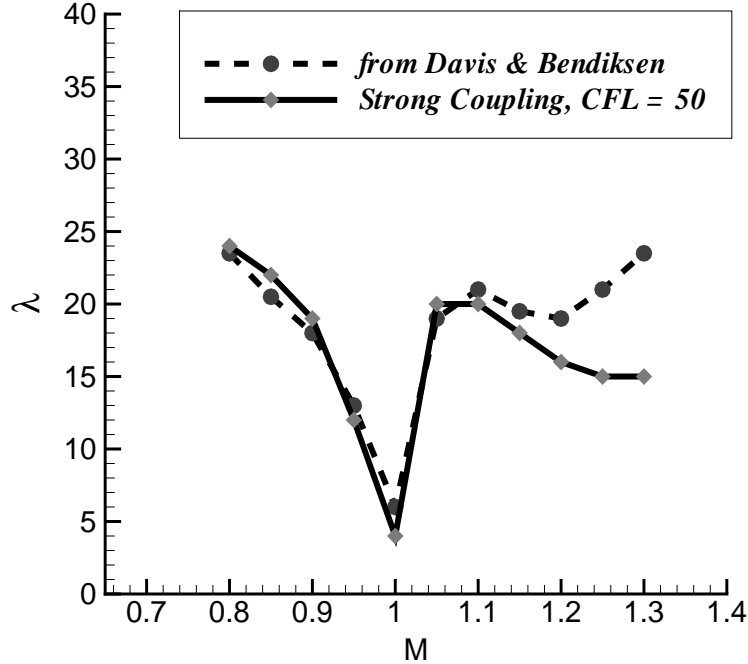
26

Figure 15: Stability boundary found here and the one from Davis and Bendiksen [5].

finally fails. The same instabilities also appear at CFL = 10. Exchanging the fluid time integrator with the mid–point rule, the time lag reduces to $\Delta t/2$ and the instabilities are triggered later.

These instabilities do not occur with the staggered coupling or the strong coupling. We show the instabilities for a physically stable case, a divergence case and a flutter case.

Applying the loose coupling with the BDF–scheme in the fluid to the case $M_\infty = 0.85$, $\lambda = 18$, Fig. 16, the mid point deflection suggests a physically stable case until $t/t^* = 700$. When the calculations are continued, a numerical instability occurs and the algorithm fails around $t/t^* = 2700$. With the mid–point rule in the fluid the instability is triggered later. With the staggered coupling or the strong coupling the numerical instability is not present.

At $M_\infty = 0.95$, $\lambda = 13$, calculated again with the loose coupling and CFL = 50 (Fig. 17), up to a dimensionless time of 900 the obtained solution makes you believe that a divergence with small amplitude is detected. Then the deflection suddenly drops, and up to a dimensionless time of 1500 the system seems to be stable, but suddenly a numerical instability is encountered again, finally leading to the failure of the algorithm. Again, using the mid–point rule in the fluid, the instability is triggered much later

At $M_\infty = 1.25$, $\lambda = 19$ flutter occurs and a CFL number of 50 corresponds to 25 time steps per flutter period. In Fig. 18 we see that at a dimensionless time of 1300, the loose, the staggered and the strong coupling have settled to a limit cycle. A pronounced disagreement in the flutter amplitudes can be observed. Continuing the calculations, the
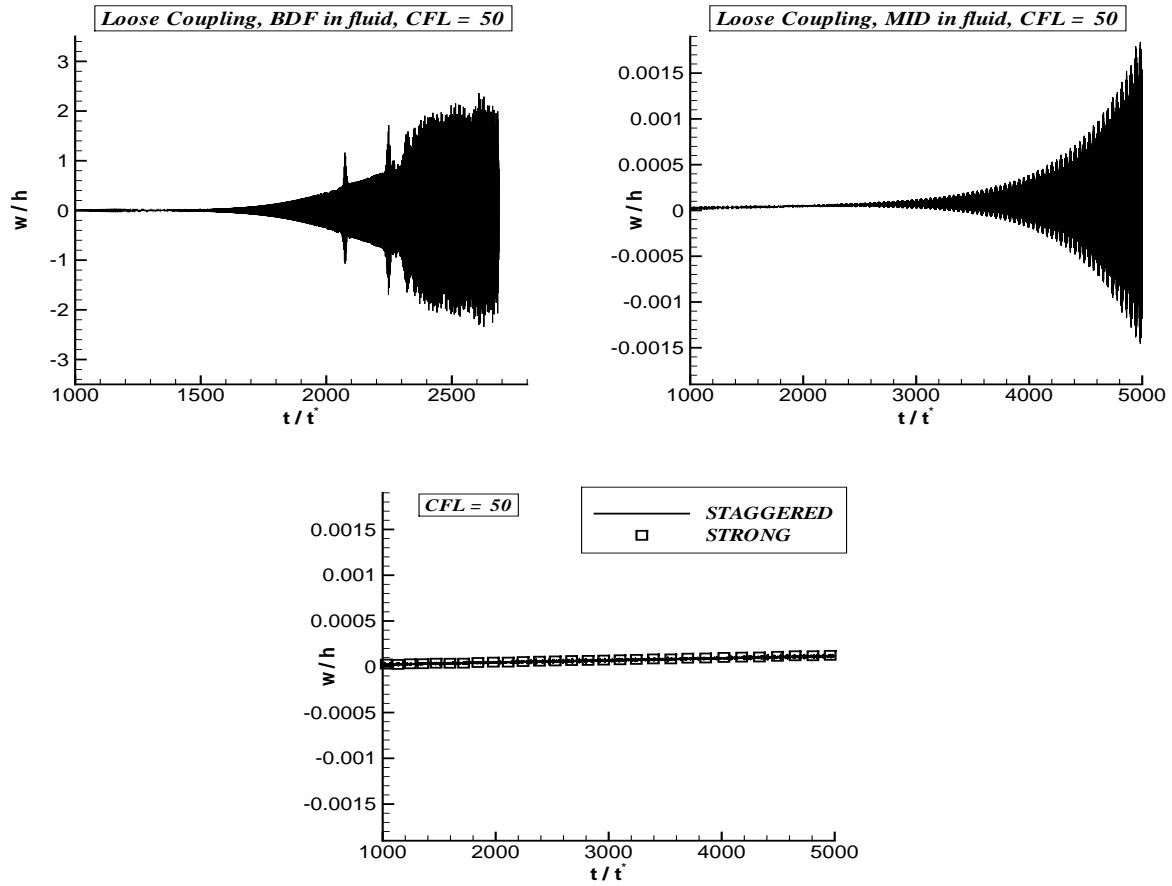
Figure 16: Numerical long time instability of loose coupling in a physically stable case. The strong and the staggered coupling both predict the same "slight divergence".
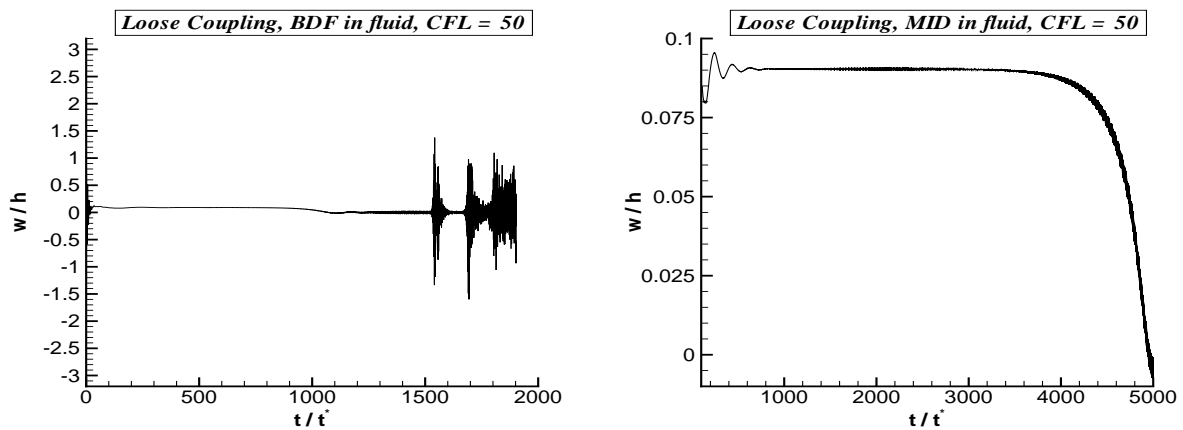

Figure 17: Numerical long time instability of loose coupling in a divergence case. The strong and the staggered coupling both predict a divergence with $w/h = 0.09$.
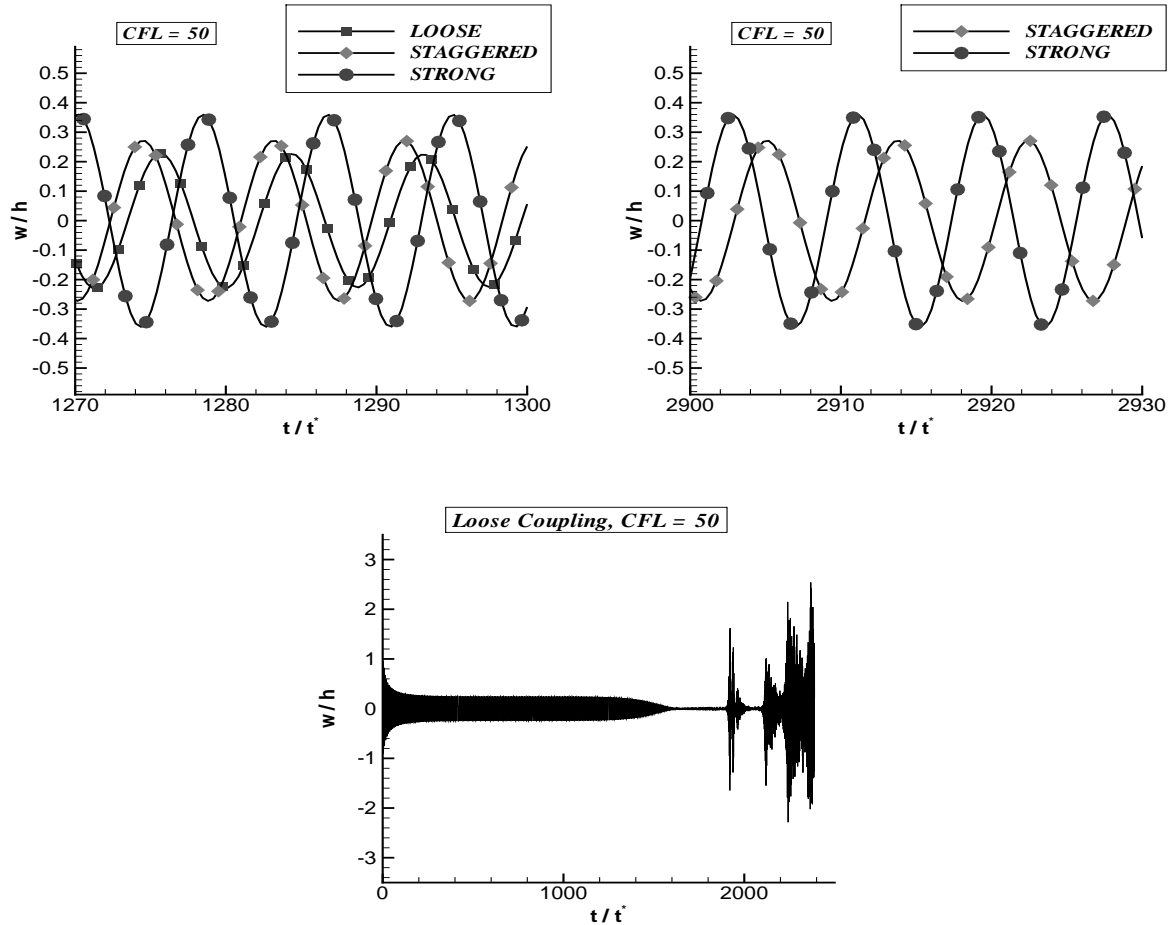
28

Figure 18: Numerical long time instability of loose coupling in a flutter case.

limit cycles are maintained in the staggered and the strong coupling. With the loose coupling the amplitude suddenly diminishes at a dimensionless time of 1600 and soon after blows up.

7   Conclusions

The panel flutter problem was considered as a model problem to investigate upon numerical methods for nonlinear aeroelastic problems. We have proposed a strong coupling to numerically solve the problem. This means that the discretization of the aeroelastic intial boundary value problem was designed such that the energy conservation property of the continuous model is carried over to the discrete model and that all discretization steps employed are of second order in time and space. The resulting scheme is implicit over the fluid and structure unknowns. A matrix–free Newton-GMRes method was proposed as a solution procedure using the separate preconditioners of the two media. A fixed point iteration is seen to be more robust and shows faster convergence. Convergence problems

29

in the fluid residual, encountered with the Newton method, could be removed by introducing a simple weighting of fluid and structure residual during the iteration process. But still the fixed point method is to be preferred. In contrast to simpler strategies such as the loose or the staggered coupling our discretization achieves a higher order in time at the fluid–structure interface. This could be demonstrated clearly through numerical experiments. The comparisons show that the loose and the staggered coupling show the same accuracy as the time step size diminishes. A striking superiority of the strong coupling over the loose and staggered coupling is observed already at moderate time step sizes in transonic aeroelastic cases with strong shocks. This was observed by numerical experiments when determining a bifurcation point in the corresponding physical regime. Further, the loose coupling exhibits a numerical long time instability. In the loose coupling, the choice of time integrators used in fluid and structure determines the time lag between the action of the pressure on the fluid and the structure. From the comparisons made,' one may conclude that the instability is triggered the sooner, the larger the time lag is. The instability was not observed with both the staggered and the strong coupling.

References

[1] J.J. ALONSO, A. JAMESON, *Fully–Implicit Time–Marching Aeroelastic Solutions.* AIAA-Paper 94-0056 (1994)

[2] O. BENDIKSEN, *A new approach to Computational Aeroelasticity.* AIAA-Paper 91-0939-CP (1991)

[3] O. BENDIKSEN, G. DAVIS, *Nonlinear Travelling Wave Flutter of Panels in Transonic Flow.* AIAA-Paper (1995)

[4] J. R. CEBRAL, R. LÖHNER, *Conservative Load Projection and Tracking for Fluid-Structure Problems.* AIAA-Journal, Vol. 35, No. 4, pg. 678-692(1997)

[5] G. DAVIS, O. BENDIKSEN, *Transonic Panel Flutter.* AIAA-Paper 93-1476 (1993)

[6] E.H. DOWELL, *Aeroelasticity of Plates and Shells.* Noordhoff International Publishing (1975)

[7] C. FARHAT, P. GEUZAINE, C. GRANDMONT, *The Discrete Geometric Conservation Law and the Nonlinear Stability of ALE Schemes for the Solution of Flow Problems on Moving Grids.* Journal of Computational Physics, 2001, 174, pg. 669-694

[8] C. FARHAT, M. LESOINNE, *On the Accuracy, Stability, and Performance of the Three-Dimensional Nonlinear Transient Aeroelastic Problems by Partitioned Procedures.* AIAA-Paper 96-1388-CP, 1996

[9] C. Farhat, M. Lesoinne, P. LeTallec, *Load and motion transfer algorithms for fluid/structure interaction problems with nonmatching discrete interfaces : Momentum and energy conservation, optimal discretization and application to aeroelasticity.* Comput. Methods Appl. Mech. Engrg., 157, pg. 95-114 (1998)

[10] R.E. Gordnier, M.R. Visbal, *Development of a three-dimensional viscous aeroelastic solver for nonlinear panel flutter.* AIAA-Paper 2000-2337 (2000)

[11] G. Guruswamy, *Coupled Finite–Difference/Finite–Element Approach for Wing–Body Aeroelasticity.* AIAA-Paper 92-4680-CP (1992)

[12] J. Hurka, J. Ballmann. *Elastic Panels in Transonic Flow,* AIAA-Paper 2001-2722 (2001)

[13] K. Isogai, *Transonic Dip Mechanism of Flutter of a Sweptback Wing: Part II.* AIAA-Journal, Vol.19, No.9, pg. 1240-1242 (1981)

[14] B. Koobus, C. Farhat, *Second-order time-accurate and geometrically conservative implicit schemes for flow computations on unstructured dynamic meshes.* Comput. Methods Appl. Mech. Engrg., 170, pg. 103-129 (1999)

[15] Ilan Kroo, *http://aero.stanford.edu/StdAtm.html*

[16] M. Lesoinne, C. Farhat, *Geometric conservation laws for flow problems with moving boundaries, and their impact on aeroelastic computaions.* Comput. Methods Appl. Mech. Engrg., 134, pg. 71-80 (1996)

[17] S. Morton, R. Melville, M. Visbal, *Accuracy and Coupling Issues of Aeroelastic Navier–Stokes Solutions on Deforming Meshes.* Journal of Aircraft, Vol. 35, No.5, pg. 798-805 (1998)

[18] S. Piperno, *Explicit/Implicit Fluid/Structure Staggered Procedures with a Structural Predictor and Fluid Subcycling for 2D Inviscid Aeroelastic Simulations.* Int. J. Num. Meth. Fluids, 25, pg. 1207-1226 (1997)

[19] N. Qin, D. Ludlow, S. Shaw, *A matrix-free preconditioned Newton/GMRES method for unsteady Navier-Stokes solutions.* Int. J. Num. Meth. Fluids, 33, pg. 223-248 (2000)

[20] Y. Saad, *Iterative methods for sparse linear systems.* PWS Publishing, New York (1996)

[21] K. Thompson, *Time Dependent Boundary Conditions for Hyperbolic Systems.* Journal of Computational Physics, 68, pg. 1-24 (1987)